

Wetting morphologies and their transitions in grooved substrates

This content has been downloaded from IOPscience. Please scroll down to see the full text.

2011 J. Phys.: Condens. Matter 23 184108

(<http://iopscience.iop.org/0953-8984/23/18/184108>)

View [the table of contents for this issue](#), or go to the [journal homepage](#) for more

Download details:

IP Address: 131.252.200.205

This content was downloaded on 02/12/2016 at 22:53

Please note that [terms and conditions apply](#).

You may also be interested in:

[Patterning of polymers: precise channel stamping by optimizing wetting properties](#)

Ralf Seemann, Edward J Kramer and Frederick F Lange

[Slip effects in polymer thin films](#)

O Bäumchen and K Jacobs

[Electrowetting: from basics to applications](#)

Frieder Mugele and Jean-Christophe Baret

[Dynamics and structure formation in thin polymer melt films](#)

Ralf Seemann, Stephan Herminghaus, Chiara Neto et al.

[Roughness-induced superhydrophobicity: a way to design non-adhesive surfaces](#)

Michael Nosonovsky and Bharat Bhushan

[Dynamics of wetting: from inertial spreading to viscous imbibition](#)

L Courbin, J C Bird, M Reyssat et al.

[Slippage and nanorheology of thin liquid polymer films](#)

Oliver Bäumchen, Renate Fetzer, Mischa Klos et al.

[Wetting, budding, and fusion—morphological transitions of soft surfaces](#)

Reinhard Lipowsky, Martin Brinkmann, Rumiana Dimova et al.

[Dynamics of nanodroplets on topographically structured substrates](#)

A Moosavi, M Rauscher and S Dietrich

Wetting morphologies and their transitions in grooved substrates

Ralf Seemann^{1,2}, Martin Brinkmann², Stephan Herminghaus²,
Krishnacharya Khare², Bruce M Law³, Sean McBride³,
Konstantina Kostourou², Evgeny Gurevich², Stefan Bommer¹,
Carsten Herrmann¹ and Dominik Michler^{1,2}

¹ Experimental Physics, Saarland University, D-66123 Saarbrücken, Germany

² Max Planck Institute for Dynamics and Self-Organization, D-37073 Göttingen, Germany

³ Department of Physics, Kansas State University, Manhattan, KS 66506, USA

E-mail: r.seemann@physik.uni-saarland.de

Received 7 December 2010, in final form 3 February 2011

Published 20 April 2011

Online at stacks.iop.org/JPhysCM/23/184108

Abstract

When exposed to a partially wetting liquid, many natural and artificial surfaces equipped with complex topographies display a rich variety of liquid interfacial morphologies. In the present article, we focus on a few simple paradigmatic surface topographies and elaborate on the statics and dynamics of the resulting wetting morphologies. It is demonstrated that the spectrum of wetting morphologies increases with increasing complexity of the groove structure. On elastically deformable substrates, additional structures in the liquid morphologies can be observed, which are caused by deformations of the groove geometry in the presence of capillary forces. The emergence of certain liquid morphologies in grooves can be actively controlled by changes in wettability and geometry. For electrically conducting solid substrates, the apparent contact angle can be varied by electrowetting. This allows, depending on groove geometry, a reversible or irreversible transport of liquid along surface grooves. In the case of irreversible liquid transport in triangular grooves, the dynamics of the emerging instability is sensitive to the apparent hydrodynamic slip at the substrate. On elastic substrates, the geometry can be varied in a straightforward manner by stretching or relaxing the sample. The imbibition velocity in deformable grooves is significantly reduced compared to solid grooves, which is a result of the microscopic deformation of the elastic groove material close to the three phase contact line.

(Some figures in this article are in colour only in the electronic version)

1. Introduction

Solid surfaces decorated with complex surface geometries on the sub-millimeter length scale exhibit unusual wetting properties: surfaces of a moderately hydrophobic material can become highly water repellent when decorated with a pattern of microscopic pillars [1–3]. The water repellent properties became famous from the lotus effect, named after the water repellent and self-cleaning properties of leaves of the lotus plant [1], which has meanwhile been adapted to numerous technological products such as paints and coatings. This water repellent situation of a droplet sitting on several pillars or ridges is called the Cassie state [4]. However, for increasing wettability or different geometry of the topography, droplets

might rather sit between multiple pillars or grooves, and the effective wettability in this case is increased by the topography. This situation is called the Wenzel state [5]. The emerging wetting morphologies in the Cassie and the Wenzel state and the intermediate situations between Cassie and Wenzel states have been studied frequently in the past [6–11].

In all of the above-mentioned cases, the footprint of one droplet spans the area of many pillars or topographic features, thus experiencing not local but averaged wettabilities. In the present article, we will exclusively study topographies which are translationally invariant in one direction. If the characteristic size of a droplet ($\sim \sqrt[3]{\text{volume}}$) is reduced, local wettabilities govern the drop shape, i.e. the droplet becomes faceted and aligns with the direction of, for example, the

grooves [12–14, 7, 6, 15–18]. Upon reducing the droplet size even further to be about equal to the characteristic length scale of the topographic feature, a variety of different liquid morphologies can be found within a single groove. The emerging wetting morphology depends on the particular wetting properties of the system and the particular geometry of the topography. This can be seen, for example, from the spontaneous organization of liquids into a large variety of different droplet shapes in the presence of surface topographies during condensation or dewetting [19–25]. The types of wetting morphologies are relevant to the function of many biological surfaces, since plants are often equipped with a complex texture of elastic hydrophobic microstructures [1, 23, 26–30], which repel the liquid or guide it to desired areas. The interplay between surface geometry and wettability is also important in many technical applications such as, for example, controlled spreading of soldering fluid or glue along grooves and wedges [31–37], to the wettability and cleanability of fabrics [38, 39], or how liquids adhere to human skin [40]. Topographically structured substrates can also be employed as passive interfaces between closed microfluidic systems in lab-on-a-chip applications and the outside world. In such an interface the liquid is driven solely by capillary action. In this paper we discuss the emerging liquid morphologies in grooves of a few paradigm geometries. We begin with infinite wedges, i.e. wedges with infinitely long side walls, which have the simplest topography and increase the complexity by adding corners and edges leading to steps, triangular, rectangular, and trapezoidal grooves. On elastic substrates, the ridges forming the grooves might be deformable, such that the emerging liquid morphologies influence the geometry of the groove by virtue of capillary forces, leading to additional wetting patterns.

When combined with the means to either vary the wettability or geometry of the substrate, liquid can be actively transported along specifically designed surface topographies. On solid substrate we switch between different wetting morphologies by changing the apparent contact angle using the electrowetting-effect on dielectric [41–46] and study the emerging reversible and irreversible filling transitions. From a detailed analysis of the dynamics of the irreversible transition between different liquid morphologies we can even probe physical properties of the liquid/solid interface, i.e. the hydrodynamic boundary conditions (slip/no-slip) of the liquid at the substrate. Using elastic substrates, we switch between different liquid morphologies by changing the geometry through stretching or relaxing the grooved substrate. The dynamics of this approach reveals that again microscopic features at the three phase contact line, i.e. small deformations of the elastic substrates, dominate the dynamics of this process.

The statics and dynamics of wetting droplets with a size between a few tens of nanometers and a millimeter are solely governed by interfacial energies. In this range of small length scales, gravity and interfacial forces, like van der Waals forces, can be safely neglected. The wetting liquids are considered as non-volatile as long as the typical time scale of a measurement is fast compared to evaporation or condensation. This implies that the capillary model applies to these systems without further restrictions and the free liquid interface of a static droplet will be a surface of constant mean curvature [47].

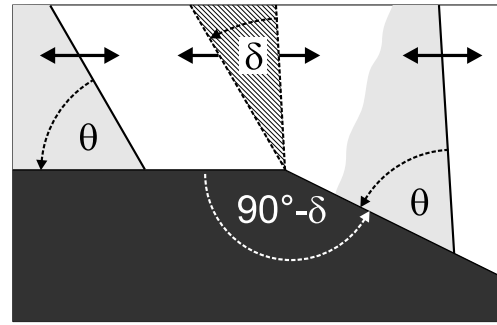


Figure 1. Contact line pinning at an ideal acute edge. In the pinned state, the slope of the liquid–vapor interface lies in the hatched sector of width δ , where $90^\circ - \delta$ is the opening angle of the solid wedge. When a liquid front moves, e.g. on the horizontal plane from left to right, it assumes the equilibrium contact angle θ . When it reaches the corner, the three phase contact line stays pinned until the contact angle reaches the angle $\theta + \delta$ to the horizontal plane, i.e. the equilibrium contact angle θ at the inclined plane.

Under these conditions a liquid droplet on an ideally smooth, chemically homogeneous and rigid surface assumes the shape of a spherical cap after mechanical equilibration. The contact angle θ , i.e. the slope of the liquid–vapor interface at the (ideal) solid, satisfies the equation of Young–Dupré [48]:

$$\gamma \cos \theta = \gamma_{sv} - \gamma_{sl}, \quad (1)$$

where γ_{sv} and γ_{sl} denote the surface tensions of the solid–vapor and the solid–liquid interfaces, respectively.

The equation of Young–Dupré (1) is only valid if the contact line is located on a smooth part of the surface. Acute edges of the substrate have the ability to immobilize the contact line. Thus, the key to understanding the large spectrum of different liquid morphologies on surfaces with complex surface geometries is the behavior of the three phase contact line at these kinks [19–21, 23, 26, 49]. If the slope of a liquid interface at the contact line located at such a kink falls into an interval limited by the slopes with respect to the equilibrium slopes (i.e. the equilibrium contact angle) to one or the other side of the kink, the contact line will be trapped in such a ‘pinned’ state [3, 50]. This situation is illustrated in figure 1 in a plane cut perpendicular to the contact line. It is shown in [51] that the threshold height of a step to cause contact line pinning of a dewetting polymer film is of the order of a few nanometers, only.

Pinning the contact line by means of surface topographies opens new degrees of freedom for the liquid–vapor interface in equilibrium. But not only the equilibrium is affected by contact line pinning: the dewetting dynamics of filamentous liquid structures in linear surface grooves is substantially different for laterally pinned or non-pinned contact lines, as we will demonstrate below.

2. Experimental details

2.1. Preparation of solid substrates

Substrates with linear triangular and trapezoidal grooves were purchased from μ Mash (Spain), Nascatec (Kassel, Germany),

and IMS (Stuttgart, Germany). The grooves were fabricated in silicon using standard photolithography and anisotropic wet etching of the mono-crystalline silicon substrates with KOH [20, 21, 52], resulting in a wedge angle of $\psi = 54.7^\circ$ with the $\langle 100 \rangle$ surface of the silicon crystal. Rectangular grooves with various aspect ratios $X = h/w$, i.e. the ratios of height to width of the channels, between $2.5 \leq X \leq 6$ and aspect ratios of the ridges separating the grooves between $0.38 \leq X_{\text{ridge}} \leq 7.71$ were purchased from Nascatec (Kassel, Germany) and IMS (Stuttgart, Germany). The rectangular grooves were also fabricated in $\langle 100 \rangle$ silicon wafers using the same photolithographic procedure but followed by an isotropic reactive (dry) etching.

In order to modify the wettability, the silicon surfaces were hydrophobized by various self-assembled monolayers (SAM) (purchased from ABCR, Germany). Octadecyltrichlorosilane (OTS) was deposited from solution [53], leading to a contact angle of $\theta = (58 \pm 1)^\circ$ for polystyrene and an excellent surface quality. To obtain larger contact angles for polystyrene, semi-fluorinated chlorosilanes, (3-Heptafluoroisopropoxy)-propyltrichlorosilane (HTS) and (Heptadecafluoro-1,1,2,2-tetrahydrodecyl)-dimethylchlorosilane (HMS) were vapor deposited onto the silicon substrate, resulting in contact angles of $(64 \pm 2)^\circ$ and $(74 \pm 2)^\circ$ for polystyrene, respectively. Intermediate contact angles were achieved at the cost of increased contact angle hysteresis by co-evaporation of either HTS or HMS with (3-Methacryloyloxypropyl)trichlorosilane (MTS) resulting in contact angles of $(57 \pm 3)^\circ$ and $(60 \pm 3)^\circ$ for polystyrene, respectively. To tune the wettability in an even wider range to achieve polystyrene contact angles between 5° and 75° , the SAM layers were treated by an oxygen plasma for a few seconds.

2.2. Preparation of rubber elastic poly-dimethylsiloxane substrates

Rubber elastic poly-dimethylsiloxane (PDMS) substrates were prepared from commercially available SYLGARD[®] 184 (SG184) and SYLGARD[®] 186 (SG186) (Dow Corning) elastomer mixtures. Planar Sylgard films of $(6 \pm 0.5) \mu\text{m}$ were prepared by spin-coating a ready prepared Sylgard mixture on previously cleaned silicon wafers which were slightly diluted with toluene to reduce its viscosity prior to spin-coating. The PDMS was subsequently cured in a protected atmosphere (N_2) at 170°C for 1 h. Surface characterization of the prepared substrates by atomic force microscopy (AFM) revealed an RMS roughness of $(0.28 \pm 0.05) \text{ nm}$. The elastic moduli of our substrates were measured to be $(5.0 \pm 0.5) \text{ MPa}$ for SG184 and $(1.5 \pm 0.1) \text{ MPa}$ for SG186 as determined by bulk rheological and thin film measurements. Elasticities between the limiting values of SG184 and SG186 were prepared by mixtures of SG184 and SG186. The equilibrium contact angle of polystyrene on PDMS was determined by AFM to be $\theta = (62 \pm 1)^\circ$ and the optically determined advancing and receding contact angle of water was determined to be $\theta_{\text{adv}} = (116 \pm 4)^\circ$ and $\theta_{\text{rec}} = (99 \pm 3)^\circ$, respectively.

Topographically structured PDMS substrates with rectangular grooves were prepared by molding SG184 against

grooved silicon substrates that were fabricated and hydrophobized using OTS as explained above.

2.3. Polystyrene as wetting liquid

As the wetting liquid, we typically used short chained atactic polystyrene (PS) purchased from Polymer Standards Service (Mainz, Germany) with a monodispersity of $M_w/M_n = 1.06\text{--}1.04$ and molecular weights ranging from $M_w = 2.25 \text{ kg mol}^{-1}$ PS(2k)— 17.4 kg mol^{-1} PS(17k). PS with molecular weights of $M_w = 2.25$ and 17.4 kg mol^{-1} are glassy at room temperature and below the entanglement length. Thus their melt can be approximately treated as a Newtonian liquid [54–56]. The surface tension of PS in air is $\gamma_{\text{PS/air}} = 32(1) \text{ mN m}^{-1}$.

The PS wetting morphologies were generated using three different methods depending on the particular experiment or substrate. Specific liquid equilibrium morphologies on topographically structured substrates were generated by condensing the PS from the vapor phase onto the sample surface [19, 21]. PS filaments in triangular grooves were prepared in a non-equilibrium morphology by directly spin-coating a PS-toluene solution onto the grooved substrates. During this spin-coating process the PS solution is removed from the ridges due to its rather large contact angle and PS deposits remain in the triangular grooves. Due to the fast evaporation of the toluene, liquid wedges with negative mean curvature are formed as a non-equilibrium morphology. The PS filling height, h , and filling width, w , in the grooves were adjusted via the spin-coating parameters and the concentration of the PS solution, respectively. Finally, thin homogeneous PS films on top of planar PDMS substrates were prepared by first spin-coating a PS-toluene solution onto a freshly cleaved mica sheet. Subsequently, the solidified PS film was floated on MilliporeTM water and picked up with the desired substrate.

2.4. Electrowetting experiments

To vary the apparent contact angle on demand we applied electrowetting on dielectric (EWOD) for certain experiments [41–46]. As wetting liquid, an electrically conducting mixture of water, glycerol, and NaCl in the weight ratio of 17:80:3 having a conductivity of $\sigma_{\text{bulk}} = (0.11 \pm 0.04) \text{ S/m}$ [57] was used, which is hygroscopically stable in our typical lab conditions.

The topographic structures that were used for the electrowetting experiments were fabricated in electrically conducting silicon as described above. Additionally, an insulating oxide layer of $d = (1.0 \pm 0.15) \mu\text{m}$ and $d = (1.15 \pm 0.15) \mu\text{m}$ was thermally grown into the silicon in the case of triangular and rectangular grooves, respectively. To render the sample hydrophobic an OTS layer was grafted onto the silicon oxide surface.

Since EWOD is not generally well known, we briefly describe the essentials here which will help in understanding the subsequent discussion: applying a voltage between a drop of an electrically conducting liquid and an electrically conducting substrate, which are separated from each other by

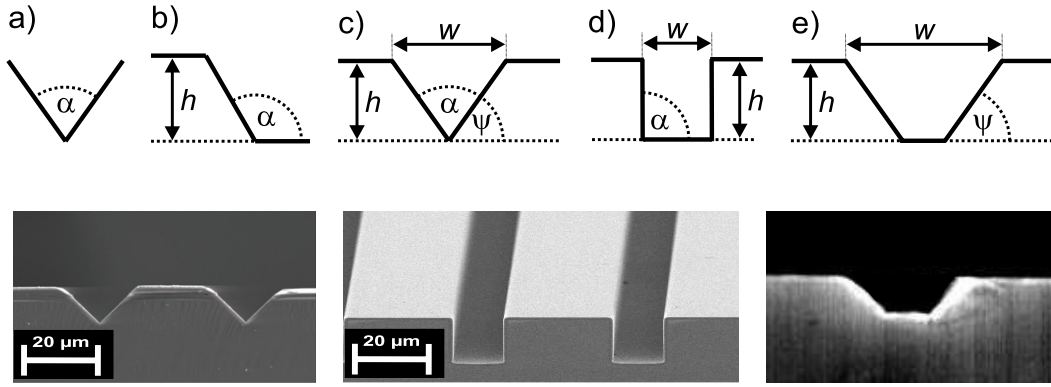


Figure 2. Top: a variety of possible polygonal cross sections for linear surface topographies, starting from an infinite wedge (a), over a topographic step (b), to grooves with triangular (c), rectangular (d), and trapezoidal cross section (e). Bottom: scanning electron micrograph of cuts through etched silicon substrates with triangular grooves (left), rectangular (middle), and trapezoidal grooves (right).

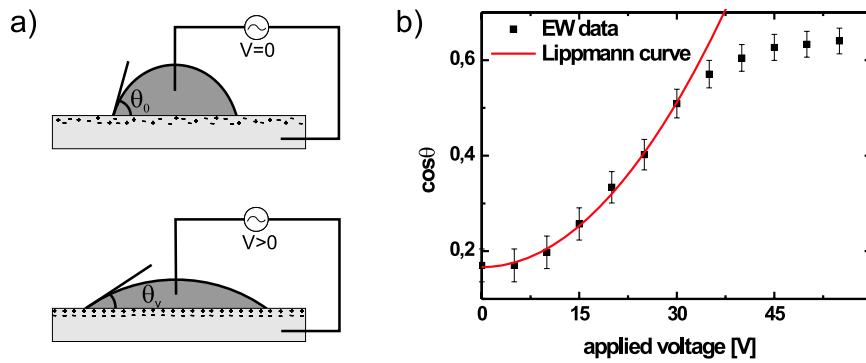


Figure 3. (a) Sketch of the electrowetting setup on dielectric (EWOD). The electrically conducting drop and the conducting silicon substrate form a capacitor with the sandwiched dielectric SiO_2 layer. Applying an electrical voltage between the drop and substrate lowers the apparent contact angle. (b) Electrowetting curve, i.e. cosine of the apparent contact angle as a function of the applied voltage, for the system used in our experiments. In the frequency range 1–30 kHz, no influence on the apparent contact angle was detectable.

a thin dielectric layer, reversibly lowers the apparent contact angle of the liquid. A typical EWOD-setup is sketched in figure 3(a). To minimize electrochemical effects, we always applied an ac voltage. The ac frequencies were in the range between $\omega = 1$ and 30 kHz. The typical dependence of the apparent contact angle on the applied voltage for the used system is shown in figure 3(b). Up to about 35 V the dependence of the apparent contact angle on the applied voltage, U , can be described by the so-called Lippmann equation

$$\cos \theta_L = \cos \theta_Y + \left(\frac{U}{U_L} \right)^2, \quad (2)$$

see, e.g. [41, 45, 46]. The characteristic voltage U_L is given by $U_L = \sqrt{2d\gamma_{lv}/\epsilon_0\epsilon_r}$, where ϵ_r is the dielectric constant of the silicon oxide layer, and ϵ_0 , the dielectric permittivity of vacuum. With our experimental system, the apparent contact angle θ_L could be tuned from about 80° without any voltage applied, down to about 45° for an applied voltage of 100 V. The apparent contact angle is independent of the frequency ω of the applied voltage and the position on the wafer.

3. Wetting of linear topographies—from wedges to trapezoidal grooves

In the following the wetting and dewetting of a few highly symmetric and paradigmatic surface topographies will be discussed. We start our discussion with equilibrium wetting morphologies that can be found in one of the most fundamental topographies, an ‘infinite’ wedge consisting of a wedge with infinitely long side walls, and increase the complexity of the topography by adding corners and edges as sketched in figure 2. As will become obvious in this discussion, the spectrum and complexity of static wetting morphologies in grooves of polygonal cross section is directly linked to the number of kinks.

3.1. Infinite wedge

The most fundamental effectively one-dimensional substrate geometry is an infinite wedge formed by two intersecting planes. Because of its invariance with respect to a rescaling in all dimensions, an infinite wedge has no intrinsic length scale and is solely characterized by the angle α between the plane walls and the wedge angle $\psi = 90^\circ - \alpha/2$, as sketched

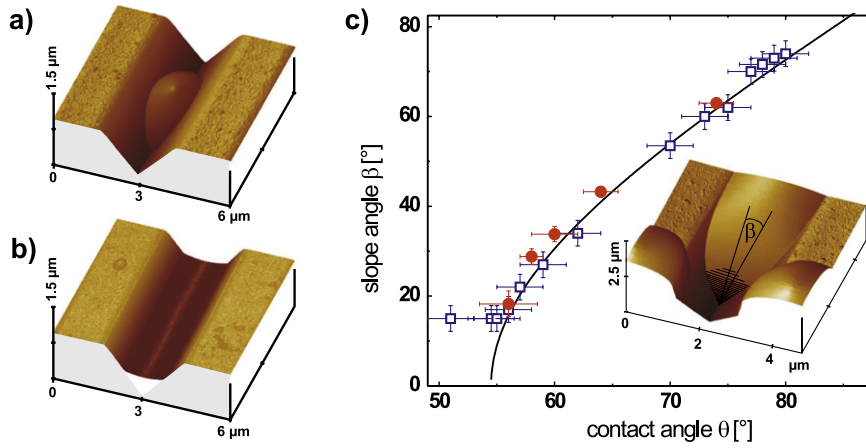


Figure 4. AFM micrographs of PS morphologies in a wedge with a wedge angle $\psi = 54.7^\circ$: (a) spherical drop with a contact angle $\theta \approx 64^\circ$; (b) liquid filament with negative Laplace pressure with $\theta \approx 33^\circ$; (c) slope angle β at the liquid tip for different contact angles θ . Data points were obtained from experiments with PS droplets (filled dots) and from electrowetting experiments (open squares). The dashed curve displays the theory of Shuttleworth and Bailey according to equations (3). Inset: AFM micrograph of the terminal meniscus of a PS droplet in a triangular groove illustrating the definition of the slope angle β .

in figure 2. Provided the liquid volume is sufficiently small and the liquid morphologies do not explore the upper edge of the groove, a triangular groove of finite width can be regarded as virtually infinite. Figure 4 shows the two static liquid morphologies that can be found in infinite wedges: droplets appear whose shape is given by segments of spheres for contact angles larger than the wedge angle, $\theta > \psi$ (figure 4(a)); and infinitely long liquid wedges appear for contact angles $\theta < \psi$ with their free liquid interface being cylindrical and always curved towards the substrate (figure 4(b)).

If we consider a droplet morphology as sketched in figure 4(a) and imagine that the contact angle θ approaches the wedge angle ψ from above, one observes a gradual elongation of the spherical drop shapes into the directions of the wedge bottom. Shuttleworth and Bailey were the first to note that the tip of a liquid filament becomes more and more pointed as the contact angle reaches the wedge angle [58]. In the limit $\theta = \psi$, the liquid extends to the entire wedge and the liquid–vapor interface attains a plane configuration [21]. One of the central assumptions of Shuttleworth and Bailey is that the liquid–vapor interface close to the tip becomes asymptotically plane, which was later rigorously proven by Concus and Finn [59, 60]. Based on their assumption, Shuttleworth and Bailey introduced a slope angle β between the free liquid interface and the bottom of the wedge and derived the relations

$$\cos \beta \cos \psi = \cos \theta \quad \text{and} \quad \tan \phi \tan \theta = \tan \beta, \quad (3)$$

which can be applied in the range of contact angles θ above the wedge angle ψ .

The left equation of (3) could be confirmed experimentally: the wettability of triangular grooves with wedge angle $\psi = 54.7^\circ$ was modified as described in the experimental section and PS was vapor condensed to form equilibrium wetting morphologies. The slope angle β at the tip of the vapor condensed morphologies was measured directly by AFM in tapping modeTM and is displayed as solid discs in

figure 4(c). PS contact angles in the range between 54.7° and about 56° closer to the wedge angle could not be achieved experimentally. Within the experimental resolution, we find perfect agreement of our experimental data with the left equation of (3). Small deviations from this behavior which are expected for a finite curvature of the bottom of the wedge are discussed in [61] but are beyond our experimental resolution.

In addition, we conducted electrowetting experiments where the contact angle of a droplet could be continuously lowered to approach the wedge angle. These experimental results agree well with both the condensation experiments and also satisfy the Shuttleworth prediction down to a slope angle of about $\beta \approx 15^\circ$ as shown by open squares in figure 4(c). The escape from the analytical model close to the filling angle is expected to result from the crossover from the apparent electrowetting contact angle according to the Lippmann equation, equation (2) to the microscopic contact angle defined by the Young–Dupré equation (1) close to the three phase contact line. The length scale of this crossover regime scales with the thickness of the insulating layer [62, 63] and agrees with the predictions based on the references [62, 63], as was shown in [21].

3.2. Topographic steps

The complexity of the wedge geometry can be further increased by adding new corners and edges. A topographic step represents the most fundamental topography beyond the infinite wedge, as sketched in figure 2(b) and is characterized by an opening angle α (or, equivalently, by the wedge angle $\psi = 90^\circ - \alpha/2$) and a step height h . In contrast to the infinite wedge geometry, the liquid volume represents a relevant control parameter for an equilibrium wetting morphology since the step height h provides an additional length scale. For small volumes and for sufficiently small contact angles, however, one expects to find liquid morphologies identical to those of the infinite wedge.

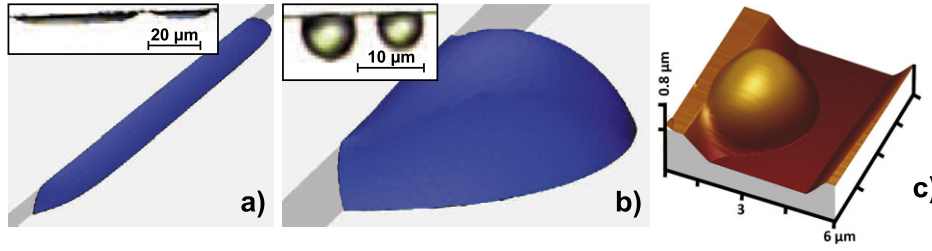


Figure 5. Numerically computed liquid filament (a) and droplet (b) wetting a topographic step with a step angle of $\alpha = 110^\circ$. The liquid volume is $V/h^3 = 25$, and the contact angle is $\theta = 40^\circ$ for the elongated filament and $\theta = 70^\circ$ for the droplet morphology. Insets: optical micrographs of PS wetting a rectangular step with (a) height $h \approx 780$ nm and contact angle $\theta \approx 41^\circ$ and (b) $h \approx 700$ nm, $\theta \approx 76^\circ$. (c) AFM micrograph of PS wetting a step with height $h \approx 565$ nm, opening angle $\alpha = 125.3^\circ$, and a contact angle of $\theta = (52 \pm 3)^\circ$.

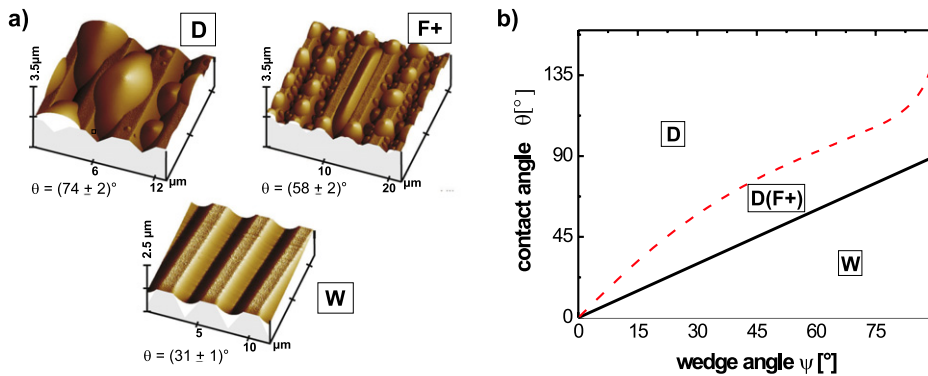


Figure 6. (a) AFM micrographs of different wetting morphologies with contact angle θ in triangular grooves with wedge angle $\psi = 54.7^\circ$. Droplet shapes are denoted with (D), liquid filaments of finite length and positive mean curvature are denoted with (F+) and infinitely long wedges are denoted with (W), respectively. (b) Morphology diagram for triangular grooves. The appearance of certain morphologies is indicated in the respective parameter regions. Brackets denote metastability of a morphology in the respective region of the diagram. The dashed line corresponds to the limit of metastability while the solid line represents the morphology transition.

If the contact angle θ exceeds the step angle ψ and if, in addition, the volume of the liquid is sufficiently large, the liquid will explore the finite vertical extension of the step. In this case, the contact line of the latter morphologies will be pinned to the upper, acute edge of the step. This allows the liquid to form elongated filaments of homogeneous cross section and positive Laplace pressure wetting a finite section of the step. Such liquid filaments with positive Laplace pressure will be found in the rather narrow range of contact angles $45^\circ < \theta \lesssim 54.5^\circ$ at a rectangular step with $\alpha = 90^\circ$ [49]. At a sufficiently high liquid volume each of these filaments is metastable with respect to a droplet whose contact line is partially pinned to the acute edge of the step. Figure 5 illustrates both types of morphologies, as obtained from numerical minimization and as observed in wetting experiments.

3.3. Triangular grooves

The spectrum of liquid equilibrium shapes in a triangular groove is also similar to that of an infinite wedge. The AFM micrographs depicted in figure 6(a) show the three principal equilibrium shapes in triangular grooves. We find elongated liquid filaments (F+) of finite length and positive Laplace pressure and almost spherical ‘overspilling’ droplets (D), wetting the groove and the plane parts of the substrate to either sides of the groove. In the range of contact angles

lower than the wedge angle $\theta < \psi$, the bottom of a triangular groove is completely wetted by single liquid filaments (W) with negative Laplace pressure. The contact line of the latter is located on the side walls of the groove. Only for finite groove length and at large filling degrees may it happen that the contact line becomes pinned to the upper groove edges for $\theta < \psi$.

The appearance of different wetting morphologies as local or global minima of the interfacial energy is illustrated in the morphology diagram shown in figure 6(b) depending on the contact angle θ and the wedge angle ψ . In the considered regime of moderately large volumes $V \gg w^3$ and $V < Lw^2$, with w being the groove width and L being the groove length, all liquid filaments with positive Laplace pressure (F+) are metastable with respect to droplets (D). The solid line in figure 6(b) separates the regions where droplets (D) or liquid filaments (W) with negative Laplace pressure are global minima of the interfacial energy. This transition line is simply given by $\theta = \psi$. The dashed line separates the region of control parameter where filaments (F+) are found as metastable minima towards large contact angles.

3.4. Rectangular grooves

The majority of static liquid morphologies found in, or on, trapezoidal and rectangular grooves are similar to those of the triangular groove [19, 21]. Both types of grooves

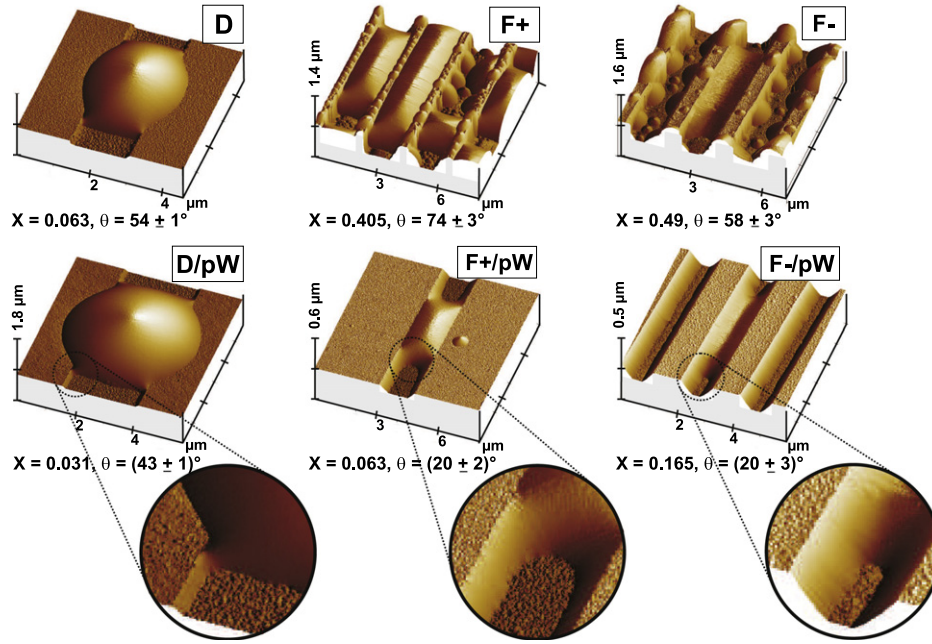


Figure 7. AFM scans of wetting morphologies at different contact angles θ in rectangular grooves of various aspect ratios X . The upper row shows liquid morphologies at contact angles $\theta > 45^\circ$. We find droplet (D) and filament morphologies. The filament morphologies might have finite length and positive (F+) or negative (F-) mean curvature. The bottom row shows morphologies for $\theta < 45^\circ$. The wetting morphologies in the bottom row spanning the entire groove width ((D, F+) and (F-)) are in coexistence with liquid protruding along the bottom corners of the wedges. We distinguish wedges that are pinned at the upper corner of the grooves as pinned wedges (pW) and wedges that are confined to the corners (cW) which emerge for large aspect ratios and low contact angles (not shown here). For better visibility we show a close up from the transition region.

can be regarded as an antisymmetric combination of two topographic steps with the same step angle. In the limit of large wall to wall separation one may consider these grooves as two individual steps being wetted by independent liquid morphologies. However, it becomes likely that liquid structures with a single meniscus spanning between the upper edges of the groove appear as the aspect ratio $X = h/w$ of groove depth h to groove width w increases. Hence an enlarged spectrum of morphologies is expected in trapezoidal and rectangular grooves [19].

Similar to the wetting morphologies in triangular grooves, the most prominent liquid equilibrium shapes in linear grooves with rectangular cross section are droplet-like shapes (D) competing with filamentous structures (F). A compilation of experimental results in rectangular grooves is shown in figure 7. We find filament structures with a single meniscus and of finite length but with either a positively (F+) or negatively curved meniscus (F-). The cross section of this type of filament is independent of the liquid volume provided the filament does not experience the finite length of the groove and depends solely on groove wettability and geometry. Hence, any increase of the liquid volume must be accompanied by an increase of its length. For contact angles below 45° we find the same liquid morphologies spanning the entire groove but now in coexistence with liquid wedges protruding along the bottom corners of the grooves, see bottom line and close ups of figure 7. The coexistence of two different wetting morphologies is in contrast to triangular grooves where only morphologies with a single meniscus are found.

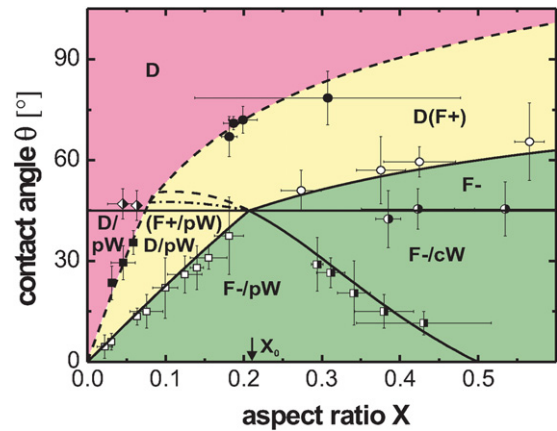


Figure 8. Morphology diagram for rectangular grooves. The abbreviations (D, F+, F-, D/pW, F+/pW, F-/pW, F-/cW) indicate the morphologies in these parametric regions; for a definition see also figure 7. Brackets denote metastability of a morphology in the respective region of the diagram. Dashed lines correspond to the limits of metastability while solid lines represent morphology transitions. The data points indicate the experimentally determined stability limits of the respective morphologies.

The appearance of certain wetting morphologies as a function of contact angle, θ , and aspect ratio of the grooves, X , can be again displayed in a morphology diagram as shown in figure 8. In the asymptotic regime of large liquid volume $V \gg w^3$, all liquid filaments (F+) are again metastable with respect to droplets (D). The dashed line bounds the region of control

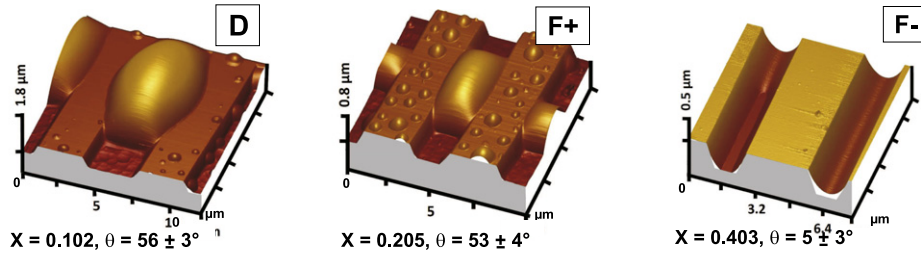


Figure 9. AFM scans of different wetting morphologies in trapezoidal grooves with wedge angle $\psi = 54.7^\circ$ at various contact angles θ and aspect ratios X . The drop (D), and filament morphologies with positive (F+) and negative mean curvature (F-) are defined as before.

parameters where filaments with positive mean curvature (F+) are found as metastable minima with respect to large contact angles. The solid line separates the regions where droplets or liquid filaments with negative mean curvature (F-) are global minima of the interfacial energy. This is fulfilled if the aspect ratio X and the contact angle θ satisfy the functional relationship $\theta = \theta_0(X)$ [19]:

$$\theta_0 = \arccos\left(\frac{1 - 4X^2}{1 + 4X^2}\right) \quad \text{and} \quad \theta_0 = \arccos\left(\frac{1}{1 + 2X}\right), \quad (4)$$

for $X < (\sqrt{2} - 1)/2 = 0.207$ and $X > 0.207$, respectively. The wetting morphologies emerging for parameters on this transition line of zero mean curvature allow us to evenly fill grooves and potentially transfer and solidify the filling liquid onto a solid substrate by techniques like channel stamping [64].

At contact angles $\theta < 45^\circ$, a new class of liquid morphologies appears in connection with the wedge geometry formed by the bottom edges of a rectangular groove. In this regime of contact angles the liquid may protrude as fine liquid filaments (W) into the edges in coexistence with the main liquid morphology. Two classes of thin liquid filaments can be distinguished: one of the two contact lines is pinned to the upper edge of the groove (pW) or both contact lines are located on the side walls (cW). Inspection of figure 8 reveals that thin liquid filaments (pW) can be found in connection with metastable filament morphologies (F+) for contact angles $\theta > 45^\circ$. In sufficiently deep grooves $X > 0.5$, however, only thin liquid filaments (cW) in combination with filaments (F-) appear below the line $\theta = 45^\circ$.

3.5. Trapezoidal grooves

For trapezoidal grooves, the appearance and the type of equilibrium wetting morphologies, see figure 9, are qualitatively identical to the morphologies found in rectangular grooves. We will thus just briefly describe the quantitative differences. For trapezoidal grooves with $\psi = 54.7^\circ$ the horizontal line at $\psi/2$ separating morphologies in coexistence with liquid wedges from those without wedges is shifted to a lower contact angle $\theta = \psi/2 = 27.35^\circ$. But not only this transition line is affected by the different angle of the side walls. All remaining transition lines are lowered accordingly. Up to an aspect ratio of $X = 0.6$, the line of zero mean curvature and the line separating the metastable filaments with positive mean curvature (F+) with respect to droplets (D) run

parallel to the respective lines for rectangular grooves, but are lowered by about 10° . These lines end at an aspect ratio of $X = (\tan \psi)/2 = 0.706$. At this aspect ratio, the two bottom corners of a trapezoidal groove merge and form a triangular cross section. Accordingly, the wetting morphologies at this aspect ratio are identical to triangular grooves. The contact angle separating the above discussed wetting morphologies can be inferred from the morphology diagram for triangular grooves for a wedge angle of $\psi = 54.7^\circ$, see figure 6.

3.6. Elastic topographic substrates

So far we considered rigid substrates which keep their shape in the presence of a wetting liquid. A number of interesting phenomena arise on substrates made from elastic materials which are soft enough to be deformed by capillary forces. In particular, we expect to see a strong influence of elasticity and substrate geometry on liquid morphologies in rectangular grooves. Unlike on rigid substrates, morphologies in adjacent grooves interact via deformations of the groove walls which lead to a lateral organization of the liquid. In the following section we will first describe static wetting morphologies in a single deformable groove and continue with a discussion of morphologies in a periodic array of adjacent grooves.

It is obvious that the influence of the capillary forces on the local groove geometry is more severe for thin ridges, i.e. ridges having a large aspect ratio⁴. However, aspect ratios larger than about six are difficult to prepare using substrates of PDMS rubber, and we restrict our discussion to grooves with a ridge aspect ratio smaller than six.

In analogy to rigid substrates, the analytical model for liquid morphologies in grooves consisting of an elastic substrate predicts overspilling droplets (D) for large contact angles. Similarly, elongated filaments whose contact line is pinned at the top corners are postulated, see figure 10. As for the morphologies found in solid grooves, figure 8, filaments can have positive (F+) and negative (F-) Laplace pressure. Provided the contact angle of the pinned meniscus is smaller than 90° , which is a necessary condition for mechanically stable filaments, the interfacial tension of the liquid/air interface gives rise to an attractive horizontal force component pulling the top ends of the ridges together. However, if the Laplace pressure resulting from the curved liquid/air interface is sufficiently large, the corresponding force can overcome

⁴ The aspect ratio of the ridge is the ratio of the ridge height to its width.

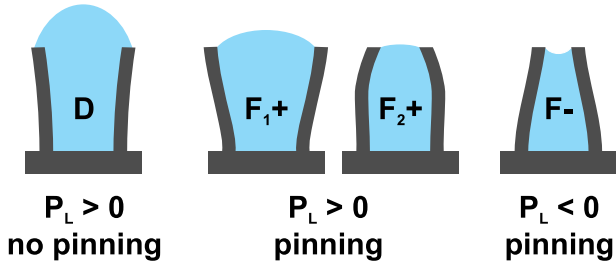


Figure 10. Sketch of morphologies that can be found in rectangular grooves made of rubber elastic material. Only droplet and filament morphologies are shown. Similar to liquid morphologies in solid grooves, we distinguish between drop morphologies (D), filaments with positive (F_+) and negative (F_-) mean curvature. Depending on groove deformation caused by the Laplace pressure and the horizontal component of the surface tension, the filaments with positive mean curvature are subdivided into (F_1+) and (F_2+).

the attractive force of the interfacial tension, resulting in an repulsive net force between the ridges. Thus, liquid filaments with positive Laplace pressure (F_+) can be subdivided into two classes, one with an increased distance of the ridges (F_1+) compared to the undeformed geometry and another where the groove ridges are pulled together (F_2+). If the Laplace pressure is negative both the horizontal component of the surface tension and the Laplace pressure in a liquid filament with negative mean curvature (F_-) exert an attractive force between the neighboring grooves and pull them closer together.

The resulting morphology diagram for rectangular grooves in an elastic substrate is similar to the one for rigid substrates, compare with figure 8. The most obvious change is that the line separating liquid morphologies with positive mean curvature from those with negative mean curvature is shifted to lower contact angles.

3.6.1. Condensation experiments. If we now consider condensation experiments in periodic groove arrays with a fairly large aspect ratio of the ridges separating adjacent grooves, it is crucial that the Laplace pressure and the surface tension acting on the ridges do not only change the cross

section of the grooves which are wetted by the liquid, but also the cross section of the two adjacent grooves. Hence a lateral ordering effect is expected during the condensation and growth of liquid structures in elastic substrates. In the presence of liquid morphologies with negative mean curvature, as is the case for highly wettable surfaces, the ridges forming the groove are pulled together due to the attractive capillary force, i.e. the groove aspect ratio is locally increased, compare with the right sketch in figure 10. As a consequence, the liquid can further increase the wetted area rendering its position energetically even more favorable (until the deformation is balanced by the elastic energy of the ridges). In contrast to that, the aspect ratio of the neighboring groove is lowered by this deformation, making it less favorable for a liquid morphology to emerge here. Similarly, a lateral ordering effect is also expected for liquid morphologies with positive mean curvature (F_+) where the local aspect ratio of a groove containing a filament is lowered, making the adjacent position of the neighboring groove energetically less favorable to form another filament (F_+).

A time series of a condensation experiment at a large material contact angle of ($\theta_{adv} = 116 \pm 4^\circ$) and ($\theta_{rec} = 99 \pm 3^\circ$) is shown in figure 11 together with the histogram of the distances between next nearest droplets for the highest ordering at the end of the condensation experiment. When the sample is cooled below the dew point, water condenses from the vapor phase at random nucleation sites, forming drop-like morphologies located in the bottom of the grooves. These droplets grow in size as the condensation continues and eventually coalesce with neighboring morphologies forming filaments with positive mean curvature of finite length. At this stage of the condensation experiment, the deformation of the ridges becomes obvious, generating filament sites which are more preferred than others. When the liquid volume of the filaments is further increased, their lateral organization is increased by pushing the existing filaments into a preferred order. As the final state of the condensation experiment we find a Gaussian type distribution of the droplet distance (in the direction of each groove) around a preferred droplet distance.

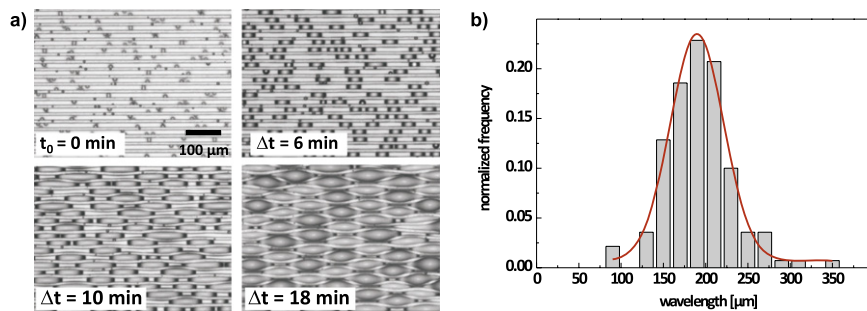


Figure 11. (a) Time series of a condensation experiment where the advancing wetting angle is $\theta_{adv} = (116 \pm 4)^\circ$ and the aspect ratio of the grooves and ridges is $X = 3$ and $X_{ridge} = 5.9$, respectively. Water is condensed from the gas phase by cooling the PDMS substrate below the dew point using a Peltier cooler. The time lapse between the first condensed droplets and the respective image is given in minutes. With increasing volume of condensed water the ordering of the emerged droplet pattern increases. The experiment is stopped when the ordering of the droplets stays unchanged for further increase of condensed water volume. (b) A histogram of the center-to-center distance of the droplets along each groove taken at the final state of the condensation experiment. The solid line shows a Gaussian fit to the data.

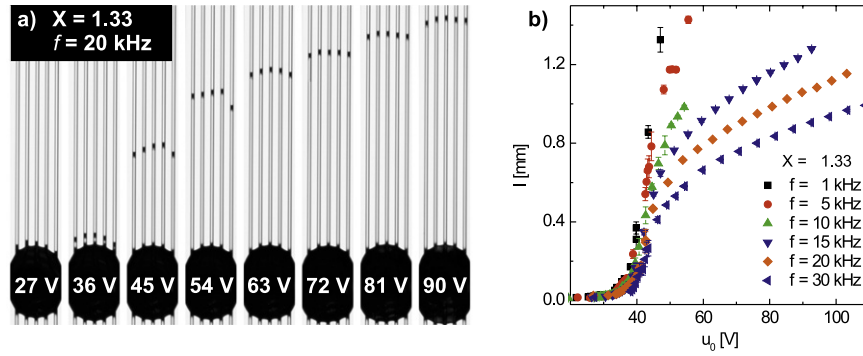


Figure 12. (a) Top-view of a droplet imbibing into grooves for different (equidistant) voltages. The tips of the liquid filaments appear black in the optical reflection micrographs. The applied voltage is given on top of the feeding drop. (b) Length of liquid filaments for different frequencies as a function of the applied voltage.

4. Switching between wetting morphologies

So far, we have discussed the spectrum of equilibrium wetting morphologies that appear in various linear rigid or elastic surface topographies at fixed wettability. The geometrical variations of the grooves in the case of elastic substrates were purely passive caused by the capillary forces of the emerging morphology. In the following section we will address morphological transitions between different liquid equilibrium shapes which are triggered externally. For rigid grooves, we induce variations of the substrate wettability by electrowetting and for elastic grooves we induce changes in the groove geometry by stretching or relaxing the elastic materials.

4.1. Groove filling and draining by variable wettability

If the contact angle θ of a droplet morphology (D) in a linear groove with given geometry is continuously lowered by electrowetting as discussed in section 2, the droplet will approach the solid line in figures 6(b) and 8 of diminishing Laplace pressure. As a result, the droplet morphology changes to a filament morphology with zero mean curvature and is drawn into the groove. Accordingly, for contact angles θ at or below the threshold angle θ_0 , liquid can be spontaneously drawn into surface grooves from a large feeding drop spanning several grooves or from any other large reservoir at virtually zero Laplace pressure. For triangular grooves, this threshold value θ_0 simply equals the wedge angle ψ of the grooves. In the case of trapezoidal and rectangular grooves, spontaneous invasion occurs at a contact angle corresponding to the transition line between droplets (D) and liquid filaments with negative Laplace pressure (F $^-$) which is given by equation (4) for rectangular grooves [19]. For trapezoidal grooves, a filling transition similar to triangular grooves is expected for large aspect ratios ($X \gtrsim 0.706$), whereas the filling transition is expected to be rather similar to rectangular grooves for small aspect ratios X .

The series of optical micrographs in figure 12(a) illustrate advancing liquid filaments in a typical filling transition of rectangular surface grooves with a groove aspect ratio of $X = 1.33$ [21, 57]. The large drop at the bottom of each image serves as a reservoir and is contacted by a platinum electrode.

The ac voltage that is applied between the aqueous liquid and the substrate is indicated on top of the respective drop and ranges up to about 100 V. For applied voltages below a threshold of about 40 V the contact angle of the liquid is lowered, but the liquid is not significantly advancing into the grooves. For applied voltages larger than the threshold, corresponding to a contact angle of about 75° , the liquid starts to invade the grooves. The length of these liquid filaments grows while the applied voltage is increased further. Due to the slanted liquid–air interface, the tips of the liquid filaments appear black in the micrographs [57]. Except for small imperfections in the grooves, all liquid filaments have the same length and their tips describe a circular arc with the same radius as the base of the feeding drop. The filament lengths as a function of the applied voltage are plotted in figure 12(b) and show a clear threshold behavior for the groove filling for various frequencies of the applied ac voltage. Provided the diameter of the feeding drop is large compared to the transverse dimensions of the groove, its Laplace pressure can be regarded as being virtually zero and the filling threshold is in agreement with the morphology diagram in figure 8, i.e. with equations (4) [19, 65].

In contrast to the expectation from the morphology diagram, the length of the liquid filaments stays finite as the voltage is increased above the filling threshold. The filament for a given applied voltage is longer the lower the frequency of the applied ac voltage. This finite length is a result of the voltage drop along the filament due to the finite conductivity of the liquid and the finite capacitive resistance of the insulating layer. It thus depends on both the frequency of the applied ac voltage and the conductivity of the liquid. The apparent electrowetting contact angle at the tip of a liquid filament equals the contact angle θ_0 of the filling transition, as shown in the morphology diagram, figure 8. Hence the voltage at the large feeding drop has to exceed the voltage at the tip (threshold voltage) to protrude a filament of finite length. In rectangular grooves, this dependence of the local voltage on the lateral position along the liquid filament is well described by a transmission line model which considers the filament as a conducting material of constant cross section surrounded by an insulating layer [21, 57]. When scaled with the frequency dependence, as given by the transmission line model, all data

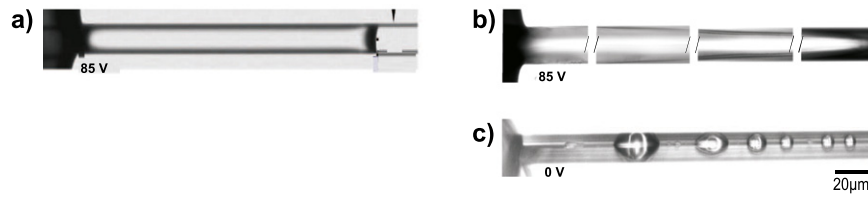


Figure 13. Single aqueous filaments drawn into grooves by electrowetting. The applied voltage is given at each filament. (a) Filaments in rectangular grooves are pinned at the upper corner of the grooves and have a constant cross section and recede fully reversibly into the feeding drop when the applied voltage is ramped down to zero. (b) Liquid filaments in triangular grooves have a free three phase contact line and a decreasing cross section towards the top of the filament. (c) When the voltage is ramped back to zero the filament decays into isolated droplets.

for different applied frequency collapse to a single master curve [57].

The filling transition of rectangular grooves is fully reversible, provided that the filaments always stay in contact with the large drop. A hysteretic transition between different liquid morphologies will occur only if the drop is completely sucked into the groove.

When the applied voltage is switched off, the dynamics of the groove draining can be quantitatively explained by a Washburn behavior [66] assuming no-slip boundary conditions at the liquid/solid interface and full slip boundary conditions at the liquid/air interface. Similarly, the imbibition dynamics can also be explained by a Washburn law if the locally varying electrowetting angle is employed in the Washburn equation [65].

Similar experiments performed with grooves of triangular cross section, however, show a remarkably different behavior: the filling threshold is not as well defined compared to the case of rectangular grooves. This can be understood by the continuous filling transition that was already briefly discussed for wetting morphologies in infinite wedges. When the contact angle is approaching the filling angle from above, elongated filaments with positive mean curvature advance into the grooves and cover the entire bottom of the groove when the filling angle is reached. Furthermore, the length of the filaments cannot be quantitatively explained by the transmission line model, assuming a constant cross-sectional area of the liquid filament.

Figure 13 shows a close up of aqueous filaments that were drawn into rectangular and triangular grooves after lowering the contact angle through electrowetting below the filling threshold. A close inspection of liquid filaments in triangular grooves, figure 13(b), reveals in fact that the contact line of the filament is not pinned and its cross section varies continuously between the tip and the feeding drop. This observation is at variance to the observations made for filaments in rectangular grooves. The latter show a discontinuous filling transition once the threshold contact angle is reached while their cross section is homogeneous along the filament except for a short region close to the liquid tip, compare with figure 13(a) [21].

An important consequence of this difference is that filling of triangular grooves is not reversible since cylindrical liquid filaments in triangular grooves with a positively curved free liquid interface and non-pinned contact lines represent mechanically unstable equilibrium shapes. This morphology

can be obtained as a transient shape if the contact angle is rapidly changed from a value smaller than the wedge angle to a value larger than the wedge angle ramping the applied voltage back to zero. As a result, the filament becomes unstable and decays in a characteristic way into a chain of isolated droplets. The final state is shown in figure 13(c), after a rapid quench from a stable liquid filament (figure 13(b)) into an unstable configuration.

4.1.1. Characteristic wavelength of instability. Due to the varying cross section of the liquid fingers which are generated by electrowetting and shown in figures 13(b) and (c) it is difficult to explore the occurring mechanical instability in detail. Thus we prepared homogeneous wedge-shaped PS filaments in a non-equilibrium situation as described in the experimental section. By heating the PS above its glass transition temperature these PS wedges relax laterally on a very short time scale and adopt the equilibrium contact angle with the solid interface of the groove walls. As a result we achieve very long PS wedges with positive mean curvature and homogeneous cross section which are mechanically unstable. An AFM micrograph of such an unstable filament is shown in figure 14(a). If we continue heating the sample the PS wedge decays into isolated droplets; an AFM image of such a droplet is shown in figure 14(b). The optical micrograph shown in figure 14(c) visualizes a larger area and demonstrates that there is a regular spacing between the resulting droplets.

The basic mechanism for the filament instability can be considered as a generalization of the Rayleigh–Plateau instability of a free-standing liquid cylinder [67]. By virtue of the wedge geometry, an increase of the filling reduces the Laplace pressure and will drive the liquid from regions with smaller filling height toward regions with larger filling height, resulting in an instability as sketched in figure 15(a).

Very short corrugations of the liquid–air interface are effectively suppressed by an additional curvature into the direction of the grooves, but all fluctuations above a certain critical longitudinal wavelength λ^* are amplified and since viscous flow resistance suppresses liquid flux over large distances, we find a wavelength $\lambda^{\max} > \lambda^*$ where the growth rate is maximal. But, in contrast to the Rayleigh–Plateau instability of a free-standing cylinder, the critical wavelength λ^* does not just depend on the diameter of the cylindrical liquid surface or the filling degree of the triangular groove. The wavelength λ^* also depends on the wedge angle and

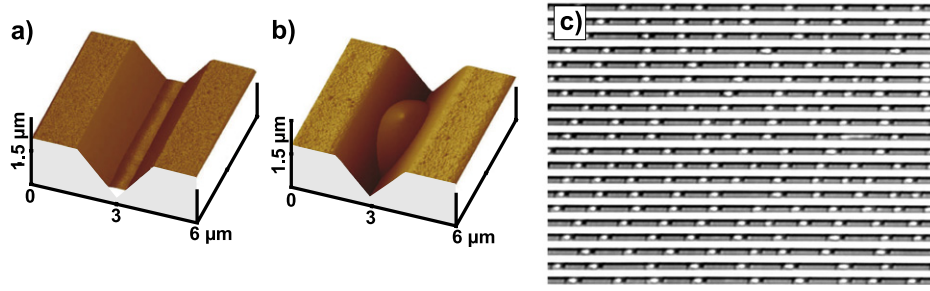


Figure 14. AFM micrographs of (a) an unstable PS filament and (b) an isolated PS droplet after filament decay. (c) Optical micrograph of PS droplets resulting from the complete decay of PS filaments.

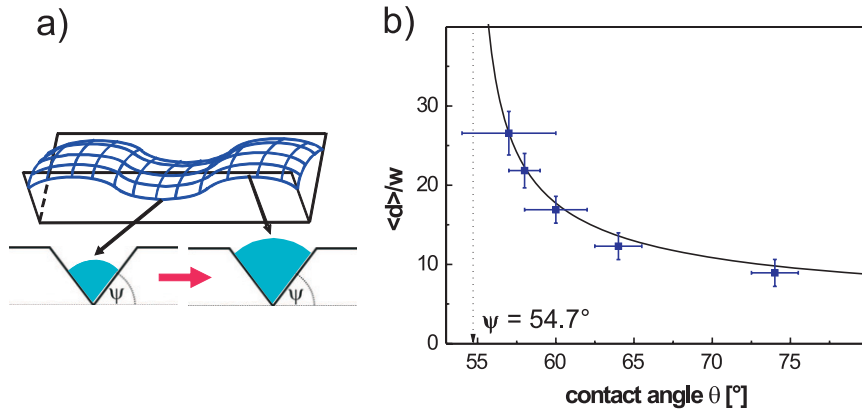


Figure 15. (a) Sketch of the filament corrugation to visualize that different filling heights result in different Laplace pressure at a given contact angle. (b) The normalized droplet distance $\langle d \rangle / w$ as a function of θ . The fastest growing mode λ^{\max} is shown as a solid line according to equation (5).

the wettability of the groove. In accordance with these expectations, the preferred wavelength λ^{\max} where the growth rate, τ^{-1} , is maximal assumes the form [20, 21]

$$\lambda^{\max} = \sqrt{2} \lambda^* = \frac{\sqrt{2} \pi w}{\sin(\theta - \psi)} \sqrt{\frac{\cos \psi - \cos \theta}{\cos \psi}}. \quad (5)$$

Considering a contact angle of $\theta = 90^\circ$, a wedge angle of $\psi = 0$, equation (5) simplifies to the known critical wavelength of the Rayleigh–Plateau instability $\lambda^* = \pi w$, where w equals the diameter of the liquid cylinder [67].

The experimental data of the preferred droplet distance $\langle d \rangle$ as a function of filling width w (not shown) corroborates the linear dependence of equation (5). The slopes of the linear fits to these data, i.e. the mean drop distances $\langle d \rangle$ normalized by the filling width w , are shown in figure 15(b) as a function of contact angle θ and also nicely reproduce the dependence of the preferred wavelength as given by equation (5).

4.1.2. Analysis of the instability dynamics. As *in situ* AFM experiments reveal, the amplitude of the preferred mode grows exponentially in time as expected from the linear stability analysis. A time series of the development of the surface corrugation is shown in figure 16(a) along with the amplitude of the fastest growing mode, as derived by Fourier analysis, which is plotted semi-logarithmically in figure 16(b).

The experimental results clearly show that this preferred wavelength prevails in the spatial pattern until the very late stage of the dewetting process [20, 21].

The experimentally determined time scale for the filament decay is determined from an exponential fit to the data, as shown in figure 16(b), and increases in a nonlinear way for increasing filament width; compare with figure 17. Assuming no-slip boundary conditions for the liquid at the solid/liquid interface, the time constant of the growth rate of the instability scales linearly with the degree of filling (at constant viscosity). For full slip boundary conditions at the solid/liquid interface we expect the mobility to diverge in our model and, hence, the time scale to become zero. But how can we understand the experimental finding shown in figure 17? Provided that the filling width is much smaller than the slip length, partial slip boundary conditions may be replaced by a full slip boundary condition. In the case of a filling height much larger than the slip length we can assume no-slip boundary conditions resulting in a vanishing time scale of the decay in this model. Hence, we expect to find a crossover from a linear scaling at large filling height to a nonlinear scaling at small filling heights. A detailed analysis of the liquid mobility reveals that the leading term in the time constant is indeed quadratic in the regime of filling heights comparable to or smaller than the slip length.

This is exactly what we found experimentally, as shown in figure 17. Knowing also the viscosity of the polystyrene,

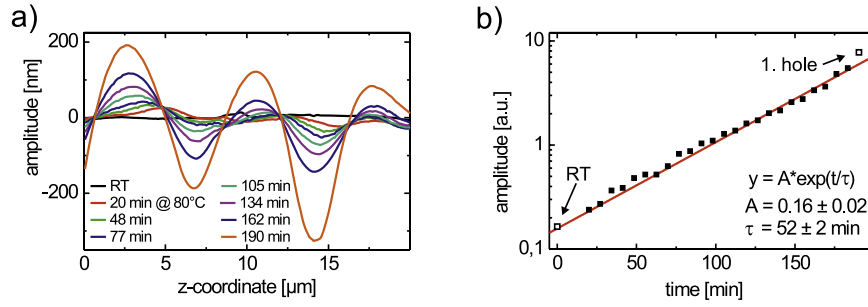


Figure 16. (a) Time series of *in situ* AFM line-scans at 80 °C showing the profile of a decaying liquid filament along the centerline of a triangular groove. (b) Amplitude of the preferred wavelength as revealed from Fourier analysis as a function of time. The marked points (corresponding to room temperature and the first hole, respectively) were not included in the fit.

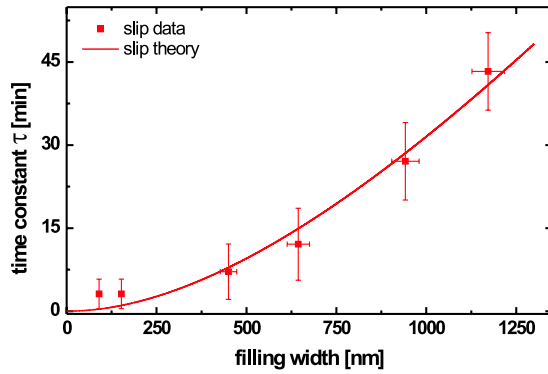


Figure 17. Exponential growth rate of filament instability as a function of the filament width as determined from *in situ* AFM data as shown in figure 16.

we can quantitatively determine the slip length by fitting our theoretical expectations to these data. For PS(18k) dewetting in HMS coated silicon grooves at a temperature of 115 °C, we determine a slip length of $b = (480 \pm 30)$ nm. Considering the increased surface roughness of the groove walls due to the etching process, this slip length is in fair agreement with the slip length of $b = (630 \pm 80)$ nm determined from rim profiles of the same polymer dewetting from a planar silicon substrate with the same surface coating at the same temperature. For the latter analysis we followed the procedure published in [54, 68–70] and nicely reviewed in [71].

4.2. Groove filling and draining by variable geometry

In section 4.1 we discussed the possibility of switching between different wetting morphologies appearing in solid substrates by changing the apparent contact angle. In terms of the morphology diagrams figures 6(b) and 8, we moved along virtual vertical lines at a fixed geometry. If the contact angle is, e.g., lowered below a threshold angle θ_0 where the corresponding equilibrium morphology approaches zero mean curvature, liquid imbibes the grooves from a large feeding drop.

Using elastic substrates allows us to modify the geometry of the grooves at fixed wettability and we can move horizontally in the morphology diagrams figures 6(b) and 8.

Similar to the case of variable wettability, we can switch between different equilibrium morphologies if we cross the solid line of diminishing Laplace pressure and can thus transport liquid along grooves. This can be achieved in a straightforward manner by employing grooved PDMS rubber substrates which can be stretched and relaxed perpendicularly to the groove direction. For sessile droplets spanning several fairly shallow grooves, this method has already been demonstrated for sinusoidal surface corrugations in [15, 18].

If we consider not only the filling threshold but also the spreading of the liquid fingers into rectangular grooves with larger aspect ratio X and not too thick ridges in more detail we encounter two particular features that are visible in figure 18. The most striking one is that the length of the advancing liquid filaments alternates, in contrast to filaments advancing in solid grooves that all had the same length, compare with figure 12(a). It seems that it is not preferred for a liquid filament to have its tip at the same lateral position as a neighboring filament. The reason for this behavior is presumably identical to the lateral ordering effect of vapor condensed drops as already described in section 3.6: the threshold for filaments to advance into the grooves is identical to the condition to find a filament with zero Laplace pressure in the grooves. This means that a liquid filament exerts a positive net interaction between the two neighboring ridges which eventually lowers the filling threshold. Assuming an ideally straight front of the liquid reservoir, the interaction between all neighboring ridges at the same filament length is identical. However, this equilibrium is unstable and due to fluctuations or due to a not perfectly straight front of the reservoir, one filament will be slightly ahead of the neighboring one and thus increase its groove aspect ratio, leading to a faster imbibition than in a neighboring filament whose groove aspect ratio is decreased. This effect should result in an alternating length of neighboring liquid filaments, similar to the observed alternating order of the vapor condensed droplets.

The second striking feature is the dynamics of the liquid imbibition. If we compare the average speed of liquid filaments advancing into grooves of solid silicon and elastic PDMS substrates both having identical geometry, the same absolute size, and about identical wettability, we find that the dynamics in elastic grooves is significantly reduced compared to the advancing dynamics in solid grooves, compare with figure 18(b).

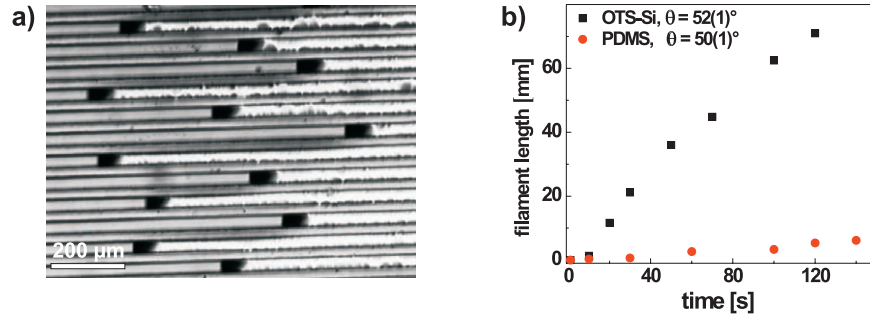


Figure 18. Optical micrograph of liquid filaments (tetraethylene glycol dimethyl ether (TEGDE) invading rectangular grooves in PDMS rubber (Sylgard 184). The filling transition was induced by stretching or relaxing the substrate perpendicular to the direction of the grooves. The contact angle of the liquid is $(50 \pm 1)^\circ$. (b) Length of the liquid filaments invading rectangular grooves of the same size, geometry, and almost identical wettability in a rigid, OTS covered silicon substrate (squares) in comparison to the elastic PDMS (Sylgard 184) substrate (dots).

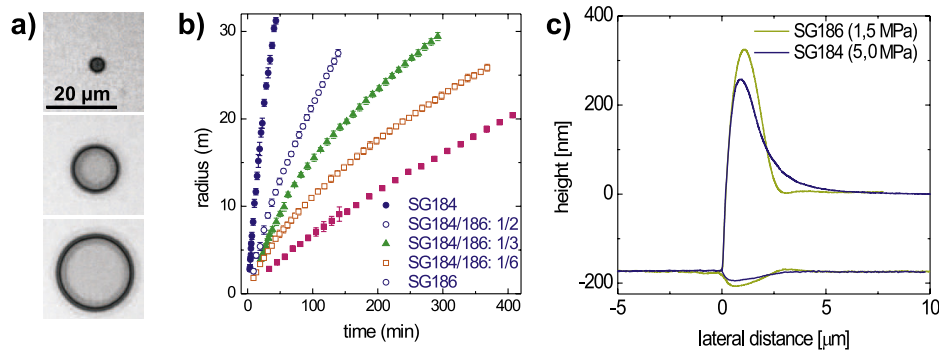


Figure 19. (a) Time series showing a PS film dewetting from a PDMS substrate. (b) Dynamics of PS(18k) with a film thickness of 150 nm dewetting from PDMS substrates at 120° . The elastic modulus varies from 1.5 MPa for Sylgard 186 to about 5 MPa for Sylgard 184. (c) Rim profiles at the same experimental conditions dewetting from Sylgard 184 and 186.

To find a possible reason for the reduced imbibition dynamics in elastic grooves we start our discussion with the known microscopic substrate deformations close to the three phase contact line. The elastic substrate is pulled upwards by the vertical component of the capillary forces acting at the three phase contact line. This effect has already been calculated for static sessile droplets [72, 73]. It was suggested that a possible viscoelastic hysteresis might influence the spreading dynamics. Experimental results on the anomalous spreading dynamics of liquid drops due to viscoelastic dissipation at the three phase contact line have been presented since then and discussed in terms of the theoretical expectations [74–77]. Based on these experimental and theoretical results, Long *et al* compared the spreading dynamics of liquids on rubber of different rheological properties and proposed a more precise theoretical description of the ‘viscoelastic braking’ [78]. The effect of ‘viscoelastic braking’ has been demonstrated also for fairly large droplets sliding down inclined rubber planes with various rheological properties driven by gravity [79]. The existence and shape of such an elevated rim around a sessile droplet has been confirmed and determined experimentally at the dry side of the three phase contact line [77, 80, 81]. Recent experimental results could also unravel the deformation which a sessile droplets causes to a rubber substrate it is sitting on at the wet side of the three phase contact line [82]. However, due

to the applied optical technique the lateral resolution is also on an optical scale.

To shed some more light on the reduced imbibition dynamics on elastic substrates and the deformation near to the advancing three phase contact line, we explored the dynamics of thin PS films dewetting from different PDMS substrates. The wettability of the various PDMS substrates remains unchanged but the elastic modulus is varied by a factor of about three between Sylgard 184 and Sylgard 186. Intermediate elasticities were prepared by mixtures of Sylgard 184 and 186, as explained in the materials section. The dewetting dynamics, i.e. the radii of growing holes in an initially homogeneous PS film are plotted in figures 19(a) and (b) showing a strong dependence on the substrate’s elastic modulus. The dewetting dynamics is slower the softer the substrate. For an increase of the elastic modulus by about three times, the dewetting velocity is increased by about 15 times.

Using a lift-off technique, we could infer experimentally the three-dimensional profile of the dewetting rims; figure 19(c)) shows an example of a PS rim profile dewetting from the softest rubber substrate in comparison with a rim profile found on our stiffest substrate at identical experimental conditions. We find that the rim profile dewetting from the softer substrate is more symmetric and a depression of the profile is observed on the wet side of the rim where the rim

decays into the initially prepared film thickness. For both substrates, the shape of the rim profile is somehow mirrored by the profile of the liquid/rubber interface and moves and grows together with the rim profile as the dewetting process continues. The shape of the liquid/rubber interface can be explained only for very small hole sizes or very small rim profiles, by the local Laplace pressure of the rim profile acting normally to the liquid/rubber interface, as the ‘mirrored’ shape suggest. For increasing hole radii the agreement of the thus constructed elastic interface deformation with the experimentally found interface deformation is reduced and most likely one has to assume that viscous stresses also have to be included to quantitatively describe the shape of the liquid/rubber interface for larger hole radii. The importance of tangential forces is strongly suggested by the ‘depletion’ area of the substrate height close to the three phase contact line, which is clearly visible in figure 19(c) for the softer substrate. Further experimental and theoretical studies are needed to clearly identify the underlying mechanisms and to describe the deformation of the liquid/rubber interface quantitatively.

5. Conclusion

We have seen that simple topographic structures like wedges, steps, and linear grooves may render the wettability of a surface amazingly complex.

For infinite wedges, topographic steps, triangular, rectangular, and trapezoidal grooves we find droplets and filaments with positive and negative mean curvature as fundamental wetting morphologies. Depending on the geometry of the grooves, the filaments with negative mean curvature might exist with infinite or finite length. The latter morphologies were found in rectangular and trapezoidal grooves. For smaller contact angles, the different wetting morphologies in rectangular and trapezoidal grooves coexist with liquid filaments which are protruding from liquid morphologies spanning the entire groove width, along the bottom corners of the grooves. The large number of different wetting morphologies is a result of the immobilization of the three phase contact line at the corners of a topographic substrate.

When liquid is condensed from the gas phase in grooves made of rubber elastic PDMS substrates, the liquid morphologies which form might deform the local geometry of the grooves. Depending on geometry, wettability, and liquid volume, drop morphologies or filament morphologies are found. Depending on the pressure inside these morphologies and the horizontal component of the surface tension, the groove walls might be either pulled towards or pushed away from the liquid morphology. This deformation might result in a laterally ordered arrangement of droplets. The typical length scale of the ordering depends on groove geometry, ridge aspect ratio, and absolute size of the grooves and ridges.

The equilibrium wetting morphologies in rigid grooves can be varied actively by varying the apparent contact angle through electrowetting for a given geometry. When the apparent contact angle is varied, the threshold for groove filling is given by the contact angle where the respective equilibrium

wetting morphologies have zero mean curvature. Applying an ac voltage for the electrowetting, the length of the filaments is finite due to a voltage drop along the liquid filament and can be described by a transmission line model. The filling threshold in rectangular grooves is discontinuous, and the spreading and receding of filaments from this reservoir is fully reversible. Using also electrowetting to vary the contact angle in triangular grooves, and also by vapor deposited PS wetting morphologies, we could demonstrate that the filling of triangular grooves is continuous. This means that a liquid filament continuously advances forward if the contact angle is decreased by increasing the applied electrowetting voltage. The cross-sectional area of this filament varies continuously from the feeding drop to the tip of the filament. When the voltage is reduced again to recede the filament back to its feeding drop, the filament may decay into isolated droplets. This break up in small droplets is similar to the Rayleigh–Plateau instability. Considering polymer filaments that were initially prepared in an unstable situation allows for a precise analysis of the wavelength and dynamics of the filament instability and lets us extract the slip/no-slip boundary conditions of the liquid/solid interface. The found surface corrugation and dynamics of a decaying filament are in good agreement with a linear stability analysis. The slip length extracted from the dynamics of the instability is also in fair agreement with different measurements using the same polymer/substrate system.

Using grooves in elastic PDMS rubber substrates, the imbibition of filaments can be triggered alternatively through variations of the groove geometry by stretching and relaxing the substrate. The filling threshold is again in agreement with the appearance of wetting morphologies with zero mean curvature. After a certain equilibration time, the length of the filaments imbibes the entire length of the groove, or is alternatively given by the volume of the feeding reservoir. The imbibition dynamics, however, is surprisingly slow in rubber elastic grooves compared to solid substrates at equal geometry and wetting conditions. In polymer dewetting experiments on planar rubber substrates, it could be shown that the dewetting dynamics slows down as the elastic modulus of the rubber decreases. This could be correlated to a remarkable deformation of the liquid/rubber interface as the dewetting front passes by. It is assumed that the viscous stresses occurring close to the three phase contact line and under the dewetting rim are responsible for this kind of braking mechanism on rubber elastic substrates.

Acknowledgments

This research was funded by the DFG priority program 1164 ‘Micro- and Nanofluidics’ under grant number Se 1118/2. S McBride and B M Law acknowledge funding from the US National Science Foundation under grant DMR-0603144.

References

- [1] Barthlott W and Neinhuis C 1997 *Planta* **202** 1
- [2] Blossey R 2003 *Nature Mater.* **2** 301

- [3] Quéré D 2005 *Rep. Prog. Phys.* **68** 2495
- [4] Cassie A B D 1948 *Discuss. Faraday Soc.* **3** 11
- [5] Wenzel T N 1949 *J. Phys. Colloid Chem.* **53** 1466
- [6] Zhao Y, Quighua L, Mei L and Xin L 2007 *Langmuir* **23** 6212
- [7] Courbin L, Denieul E, Dressaire E, Roper M, Ajdari A and Stone H A 2007 *Nature Mater.* **6** 661
- [8] Sheng Y J, Jiang S and Tsao H K 2007 *J. Chem. Phys.* **127** 234704
- [9] Koishi T, Yasuoka K, Fujikawa S, Ebisuzaki T and Zeng X C 2009 *Proc. Natl Acad. Sci. USA* **106** 8435
- [10] Gross M, Varnik F and Raabe D 2009 *Eurphys. Lett.* **88** 26002
- [11] Yong X and Zhang L T 2009 *Langmuir* **25** 5045
- [12] Darhuber A A and Troian S M 2005 *Annu. Rev. Fluid Mech.* **37** 425
- [13] Kusumaatmaja H, Vrancken R J, Bastiaansen C W M and Yeomans J M 2008 *Langmuir* **24** 7299–308
- [14] Hirvi J T and Pakkanen T A 2007 *Langmuir* **23** 7724
- [15] Khare K, Zhou J and Yang S 2009 *Langmuir* **25** 12794
- [16] Sommers A D and Jacobi A M 2008 *J. Colloid Interface Sci.* **328** 402
- [17] Yang J, Rose F R A J, Gadegaard N and Alexander M R 2009 *Langmuir* **25** 2567
- [18] Yang S, Khare K and Lin P C 2010 *Adv. Funct. Mater.* **20** 2550
- [19] Seemann R, Brinkmann M, Lange F F, Kramer E J and Lipowsky R 2005 *Proc. Natl Acad. Sci. USA* **102** 1848
- [20] Khare K, Brinkmann M, Law B M, Gurevich E, Herminghaus S and Seemann R 2007 *Langmuir* **23** 12138
- [21] Khare K, Herminghaus S, Baret J C, Law B M, Brinkmann M and Seemann R 2007 *Langmuir* **23** 12997
- [22] Narhe R D and Beysens D A 2007 *Langmuir* **23** 6486
- [23] Dorrer C and Rühe J 2007 *Langmuir* **23** 3820
- [24] Herminghaus S, Brinkmann M and Seemann R 2008 *Annu. Rev. Mater. Res.* **38** 10.1
- [25] Khare K, Brinkmann M, Law B M, Herminghaus S and Seemann R 2009 *Eur. Phys. J. Spec. Top.* **166** 151
- [26] Dorrer C and Rühe J 2007 *Langmuir* **23** 3179
- [27] Otten A and Herminghaus S 2004 *Langmuir* **20** 2405
- [28] Sun T L, Feng L, Gao X F and Jiang L 2005 *Acc. Chem. Res.* **38** 644
- [29] Blow M L and Yeomans J M 2010 *Langmuir* **26** 16071
- [30] Chu K H, Xiao R and Wang E N 2010 *Nature Mater.* **9** 413
- [31] Mann J A, Romero L, Rye R R and Yost F G 1995 *Phys. Rev. E* **52** 3967
- [32] Rye R R, Yost F G and Mann J A 1996 *Langmuir* **12** 4625
- [33] Rye R R, Mann J A and Yost F G 1996 *Langmuir* **12** 555
- [34] Yost F G, Rye R R and Mann J A 1997 *Acta Mater.* **45** 5337
- [35] Rye R R, Yost F G and O'Toole E J 1998 *Langmuir* **14** 3937
- [36] Weislogel M M and Lichter S 1998 *J. Fluid Mech.* **373** 349
- [37] Warren P B 2004 *Phys. Rev. E* **69** 041601
- [38] Hasan M M B, Calvimontes A, Synytska A and Dutschk V 2008 *Text. Res. J.* **78** 996
- [39] Hasan M M B, Calvimontes A and Dutschk V 2009 *J. Surf. Deterg.* **12** 285
- [40] Dussaud A D, Adler P M and Lips A 2003 *Langmuir* **19** 7341
- [41] Quilliet C and Berge B 2002 *Europhys. Lett.* **60** 99
- [42] Someya T, Dodabalapur A, Gelperin A, Katz H E and Bao Z 2002 *Langmuir* **18** 5299
- [43] Prins M W, Welters W J J and Weekamp J W 2001 *Science* **291** 277
- [44] Hayes R A and Feenstra B J 2003 *Nature* **425** 383
Hayes R A and Feenstra B J 2005 *Annu. Rev. Fluid Mech.* **37** 425
- [45] Lippmann G 1875 *Ann. Chim. Phys.* **5** 494
- [46] Mugele F and Baret J C 2005 *J. Phys.: Condens. Matter* **17** R705
- [47] Lipowsky R, Lenz P and Swain P S 2000 *Colloids Surf. A* **161** 3
- [48] Young T 1805 *Phil. Trans. R. Soc.* **95** 65–87
- [49] Brinkmann M and Blossey R 2004 *Eur. Phys. J. E* **14** 79
- [50] de Gennes P G 1985 *Rev. Mod. Phys.* **57** 827
- [51] Ondarcuhu T and Piednoir A 2005 *Nano Lett.* **5** 1744
- [52] Madou M J 1997 *Fundamentals of Microfabrication* (Boca Raton, FL: CRC Press)
- [53] Sagiv J 1980 *J. Am. Chem. Soc.* **102** 92
- [54] Fetzer R, Jacobs K, Münch, Wagner B and Witelski T P 2005 *Phys. Rev. Lett.* **95** 127801
- [55] Seemann R, Herminghaus R and Jacobs K 2001 *Phys. Rev. Lett.* **86** 5534
- [56] Fetzer R and Jacobs K 2007 *Langmuir* **23** 11617
- [57] Baret J C, Decré M, Herminghaus S and Seemann R 2005 *Langmuir* **21** 12218
- [58] Shuttleworth R and Bailey G L J 1948 *Discuss. Faraday Soc.* **3** 16
- [59] Concus P and Finn R 1969 *Proc. Natl Acad. Sci. USA* **63** 292
- [60] Concus P and Finn R 1974 *Acta Math.* **132** 177
- [61] Kitron-Belinkov M, Marmur A, Trabold T and Dadheech G V 2007 *Langmuir* **23** 8406
- [62] Buehrle J, Herminghaus S and Mugele F 2003 *Phys. Rev. Lett.* **91** 086101
- [63] Mugele F and Buehrle J 2007 *J. Phys.: Condens. Matter* **19** 375112
- [64] Seemann R, Kramer E J and Lange F F 2004 *New J. Phys.* **6** 111
- [65] Baret J C, Decré M, Herminghaus S and Seemann R 2007 *Langmuir* **23** 5200
- [66] Washburn E W 1921 *Phys. Rev. E* **17** 273
- [67] Rayleigh L 1878 *Proc. London Math. Soc.* **10** 4
- [68] Fetzer R, Rauscher M, Münch A, Wagner B A and Jacobs K 2006 *Europhys. Lett.* **75** 638
- [69] Fetzer R, Münch A, Wagner B, Rauscher M and Jacobs K 2007 *Langmuir* **23** 10559
- [70] Bäumchen O, Fetzer R and Jacobs K 2009 *Phys. Rev. Lett.* **103** 247801
- [71] Bäumchen O and Jacobs K 2010 *J. Phys.: Condens. Matter* **22** 033102
- [72] Shanahan M E R 1987 *J. Phys. D: Appl. Phys.* **20** 945
- [73] Shanahan M E R 1988 *J. Phys. D: Appl. Phys.* **21** 981
- [74] Shanahan M E R and Carré A 1994 *Langmuir* **10** 1647
- [75] Shanahan M E R and Carré A 1995 *Langmuir* **11** 1396
- [76] Carré A and Shanahan M E R 1995 *Langmuir* **11** 24
- [77] Carré A, Gastel J C and Shanahan M E R 1996 *Nature* **379** 432
- [78] Long D, Ajdari A and Leibler L 1996 *Langmuir* **12** 5221
- [79] Carré A and Shanahan M E R 2001 *Langmuir* **17** 2982
- [80] Extrand C and Kumagai Y 1996 *J. Colloid Interface Sci.* **184** 191
- [81] Saiz E, Tomsia A and Cannon R 1998 *Acta Mater.* **46** 2349
- [82] Pericet-Càmara R, Best A, Butt H and Bonaccorso E 2008 *Langmuir* **24** 10565